Algal Research 89 (2025) 104090

Contents lists available at ScienceDirect

Algal Research

journal homepage: www.elsevier.com/locate/algal

Non-invasive monitoring of cyanobacteria growth in a nanocellulose matrix

Tuukka Levä [a,*], Ella Mahlamäki [a], Sergey Kosourov [b], Yagut Allahverdiyeva [b], Mikko Mäkelä [a], Tekla Tammelin [a,*]

[a] VTT Technical Research Centre of Finland Ltd, VTT, PO Box 1000, FI-02044 Espoo, Finland
[b] Molecular Plant Biology, Department of Life Technologies, University of Turku, FI-20014 Turku, Finland

ARTICLE INFO

Keywords:
Cell immobilization
Solid-state photosynthetic cell factory
Chlorophyll *a*
Cellulose nanofibers
Hyperspectral imaging

ABSTRACT

Solid-state photosynthetic cell factories (SSPCFs) for sustainable chemicals manufacturing can be developed towards industrially relevant environment with rapid feedback control over their operation. This requires non-invasive monitoring of the immobilized cells in situ, which is not possible with existing methods. We deployed hyperspectral imaging in the photosynthetically active radiation range (400–700 nm) to enable such monitoring. We systematically assessed cell growth and potential stress during immobilization by studying how 2,2,6,6-tetramethylpiperidine 1-oxyl (TEMPO)-oxidized cellulose nanofiber hydrogel thickness, immobilized *Synechocystis* sp. PCC 6803 cell density and time affected the immobilized cells' absorbance spectra. Time and gel thickness together accounted for almost 80 % of the changes in the spectra. We then calibrated the imaging spectra for chlorophyll *a* to non-invasively estimate growth of healthy cells in the matrices. Promising correlation for chlorophyll *a* (model coefficient of determination, $R^2 = 0.90$) was observed between hyperspectral imaging and spectrophotometry references from methanol-extracted samples regardless of spatial differences that developed in the matrices over time. Clustering of the image pixels enabled analyzing these differences in the chlorophyll *a* concentration non-invasively from the whole matrix areas. In the future, this non-invasive data-driven method could be further developed for monitoring SSPCFs' biointelligent chemicals production, contamination, stress and cell growth.

1. Introduction

Photosynthetic microbes like microalgae and cyanobacteria produce chemicals from CO_2 in a biocatalytic conversion fueled by light. The photosynthetic machinery of these cells can be engineered by introducing new metabolic pathways with genetic and metabolic engineering [1–4]. Engineered photosynthetic cells can be further entrapped in crosslinked alginate or nanocellulose hydrogels, which are biocompatible and biodegradable immobilization matrices produced from renewable and abundant natural resources like plants and algae [5,6]. Immobilization protects the cells from adverse environmental conditions and contamination, increases volumetric cell density and restricts cell division [5–8]. Immobilization within robust matrices also improves the cells' longevity and promotes the direction of light energy and carbon towards synthesis of desired products [5–8]. We have recently established a solid-state photosynthetic cell factory (SSPCF) concept, where engineered photosynthetic cells are immobilized in thin nanocellulose matrix for sustainable production of solar chemicals and fuels [9–11]. The flat thin-layer nanocellulose matrix improves light utilization and enhances the overall photosynthetic productivity of the immobilized cells, enabling light-to-product conversion efficiencies exceeding 4 % [11]. Future SSPCFs could thus provide a key component for biointelligent manufacturing [12] of various biochemicals and biofuels in a continuous-flow system. In this realm, tailored information systems to non-invasively monitor and control the SSPCF operation are crucial. So far, promising systems for suspension-based microalgae cultivation have been reported [13–15], but they do not exist for immobilized systems yet and would require further development to be harnessed on-line during cell factory operation.

Here, we describe the first steps to develop a monitoring system for SSPCFs. We focus on monitoring chlorophyll *a*, which is a major pigment governing the efficiency of oxygenic photosynthesis and a key indicator of cell growth in plants, algae, and cyanobacteria [16]. Cell growth can be disturbed by stress, which slows down or decreases chlorophyll *a* production. Stress can occur in the immobilized cells due to various reasons. For example, transfer of gases, nutrients, or reaction substrates

* Corresponding authors.
E-mail addresses: tuukka.leva@vtt.fi (T. Levä), tekla.tammelin-peltonen@vtt.fi (T. Tammelin).

https://doi.org/10.1016/j.algal.2025.104090
Received 30 January 2025; Received in revised form 31 March 2025; Accepted 8 May 2025
Available online 9 May 2025

in an immobilized system can be slow if the immobilization matrix is too dense or thick [17–20]. This can lead to insufficient flux of photosynthetically generated oxygen out of the system, which increases the formation of reactive oxygen species and elevates the oxidative stress of the cells [21,22]. Prolonged oxidative stress can degrade chlorophyll *a*, which results in visual bleaching of immobilized cell cultures [21]. Apart from matrix thickness, high cell density can cause stress by increasing self-shading in the matrix structures, which counteracts potentially improved light-utilization efficiency of the immobilized cells [23]. Overall, stress occurs over time as the cultivation ages, and its source can change. Chlorophyll *a* is thus a potential pathway to monitor the durability of immobilized cell cultivations during SSPCF operation.

Current methods to monitor photosynthetic cells include spectroscopic measurements on whole cells [24–29] and spectrophotometric or chromatographic analyses of extracts to identify specific pigments [28,30]. Methods to determine chlorophyll fluorescence, which has a direct relationship with the efficiency of photosynthesis, are particularly common [31]. These existing methodologies may require destructive sampling in the form of extraction, labelling, or physical handling, or they can be specific for sensing certain phenomena, like chlorophyll fluorescence. Destructive sampling can disturb or disintegrate the cells and is unsuitable for operational SSPCFs. Current methodologies also fail to account for spatial features that can emerge in an immobilized solid construct. We identify a need for novel non-invasive methods to monitor SSPCFs based on chlorophyll *a* evolution without expensive and time-consuming chemical analyses.

Inspired by remote observation of plants and algae [32–35], we used hyperspectral imaging [36] to non-invasively monitor immobilized photosynthetic cells. Our objective was to assess growth of the cells and possible stress caused by immobilization. We hypothesized that hyperspectral imaging would enable us to estimate temporal chlorophyll *a* concentration across different SSPCF constructs and to potentially observe spatial differences in SSPCF features based on their pigment absorbance spectra. Thus, we studied the effects of matrix thickness, cell density and time on immobilized *Synechocystis* sp. PCC 6803 cyanobacteria by interpreting hyperspectral images determined in the photosynthetically active radiation (PAR) range within 400–700 nm. We then mathematically calibrated average hyperspectral image spectra against chlorophyll *a* concentration that was analytically determined from the cell immobilization matrices. Our work pioneers the use of hyperspectral imaging for monitoring immobilized photosynthetic cells with the ability to estimate spatial characteristics of cell growth non-invasively. In the future, such non-invasive and data-driven methodologies can help to establish SSPCFs for biointelligent chemicals production providing alternatives to traditional suspension cultures.

2. Experimental

2.1. Materials

2.1.1. Cyanobacteria and growth conditions

Wild-type *Synechocystis* sp. PCC 6803 cyanobacteria (hereafter *Synechocystis*) were cultivated in BG-11 growth medium [37]. The growth medium was buffered with 5 mM 4-(2-hydroxyethyl)-1-piperazineethanesulfonic acid (HEPES)-NaOH to maintain a steady pH of 7.5 during cell growth. The 50 ml stock culture was started at the lag phase, where the optical density of the culture at 750 nm (OD_{750}) was below 0.1 as measured with an ultraviolet-visible (UV-VIS) spectrophotometer using a 1 cm cuvette. The culture was placed on an orbital shaker (110 rpm) and incubated at 23 °C under air atmosphere and 16 h photoperiod for approximately 2 weeks. The stock culture was then used to start a 500 ml culture with aeration and 30 °C incubation temperature. This culture was maintained for 1 week, after which it was stopped at OD_{750} of 3.6 and the cells were harvested by centrifugation for immobilization via gel entrapment. Correlation of *Synechocystis* cell dry weight (CDW) with OD_{750} [23] was used to approximate immobilized cell densities in g_{CDW}/l based on the optical densities of the concentrated cell suspensions. Thereby, measured OD_{750} of 5 corresponded to approximately 1.2 g_{CDW}/l, and OD_{750} of 11 to 2.6 g_{CDW}/l. All cultures were illuminated with fluorescent lamps (Philips Master TL5 HO 39 W/865) supplying the cells with approximately 50 μmol photons m^{-2} s^{-1} PAR. All handling of the axenic cell cultures was done aseptically in an open laminar flow cabinet with sterile tools.

2.1.2. TEMPO-oxidized cellulose nanofibers (TCNF)

TEMPO-oxidized cellulose nanofibers (TCNF) were manufactured from never-dried softwood pulp (a mixture of spruce and pine). Pulping was carried out in a Finnish pulp mill and the following TEMPO-catalyzed oxidation was made with alkaline hypochlorite as the primary oxidant [38]. The chemicals used in the TEMPO-catalyzed oxidation of the pulp were 2,2,6,6-tetramethylpiperidine 1-oxyl (TEMPO) (Sigma-Aldrich, St. Louis, MO, the United States) and 10 % sodium hypochlorite (Sigma-Aldrich, St. Louis, MO, the United States). An anionic charge of 1.45–1.52 mmol/g was subsequently measured for the oxidized pulp with conductometric titration [39]. After washing, the oxidized pulp was fibrillated into TCNF by passing it twice through a microfluidizer (Microfluidics Int., Westwood, MA, the United States) with two Z-type chambers, diameters of which were 400 μm and 100 μm, at the pressure of 1850 bar. Highly transparent TCNF with 1.08 wt% solids and viscous characteristics was obtained. The chemical composition, morphology and visual outlook of the TCNF-grade used here for cell immobilization purposes have been presented earlier [6,9].

2.1.3. Other chemicals and materials

Ultrapure Milli-Q water (18.2 MΩ cm, QPAK® 1, MilliporeSigma, Burlington, MA, the United States) was used in the preparation of solutions. Calcium chloride ($CaCl_2$) (99 %, #C7902, Sigma-Aldrich, St. Louis, MO, the United States) was dissolved in Milli-Q water to obtain 50 mM solution used in the crosslinking of the cell immobilization matrices. A commercial polytetrafluoroethylene (PTFE) film (Etra Oy, Helsinki, Finland) with 100 μm thickness was used as a support during the preparation of the cell immobilization matrices.

2.1.4. Preparation and handling of the cell immobilization matrices

The cells were immobilized in biobased hydrogel matrices prepared from Ca^{2+}-crosslinked TEMPO-oxidized cellulose nanofibers, a type of nanocellulose that has excellent optical and mechanical properties for cell immobilization purposes [6,20,38]. The preparation of hydrogel immobilization matrices and cell immobilization were done in three main steps: 1) mixing of the matrix materials, 2) casting of the hydrogel and 3) re-wetting after partial dewatering of the matrix, which have been thoroughly described earlier [20]. Before the re-wetting stage, the ready samples, i.e., 2 circular pieces with a diameter of 9 cm for hyperspectral imaging and multiple 1 cm × 1 cm rectangular pieces for reference measurements, were cut from the hydrogels and fully immersed to 25 ml of BG-11 in Petri dishes. One hyperspectral imaging sample was stored per Petri dish, whereas all the hydrogel pieces for reference measurements per sample type were stored in the same Petri dish. The growth medium was changed on the first, the 10th and the 20th day after immobilization in conjunction with the time variable on the experimental design. Old media was first removed with sterile tools. Then the experiments were conducted, and new sterile media was added to the Petri dishes. Between the experiments, the samples were stored at ~28 °C, under ~50 μmol photons m^{-2} s^{-1} light input, and 16 h photoperiod in a closed Petri dish to prevent evaporation of the growth medium and contamination of the samples. The light was supplied with two 60 cm LED strips (15 W, 6400 K, 1500 lm, Nelson Garden, Tingsryd, Sweden).

2.2. Methods

2.2.1. Design of experiments

The factors controlled in the experimental design were time after immobilization (time), initial immobilized cell density in grams of cell dry weight per liter (cell density), thickness of the immobilization matrix (gel thickness) and replicate for hyperspectral imaging (replicate). A 2^3 factorial design was constructed for factors cell density, gel thickness and replicate. The factor levels were set to 1.2 and 2.6 g_{CDW}/l for cell density and 0.5 and 1 mm for gel thickness. Categorical labels 1st and 2nd were set as replicate factor levels. By considering all combinations of the controlled factors and their levels according to the experimental design, 8 physical samples with immobilized cells were prepared. These samples were then imaged with a hyperspectral camera or used in the reference measurements in three different times, 1, 10 and 20 days after their preparation, which were the predetermined levels for the controlled factor time. The factor levels for time, cell density and gel thickness were selected based on our earlier research, where good mechanical properties of the nanocellulose-based immobilization matrices [20], and excellent cell factory performance during ethylene bioproduction cycles of 5–8 days (ethylene yield >150 μmol (mg Chl)$^{-1}$) were achieved [9,10]. All experiments based on the design matrix were conducted with hyperspectral imaging, which resulted in spectra from a total of 24 experiments. Spectrophotometric determination of chlorophyll *a* from methanol-extracted samples was carried out as a reference for the hyperspectral imaging. The reference measurements were conducted with independent technical replicates that were separate from the hyperspectral imaging samples. Thus, the factor "replicate for hyperspectral imaging" was omitted for the reference method. A summary of the design of experiments is shown in the Supporting information (Table S1).

2.2.2. Hyperspectral imaging

Hyperspectral imaging measurements were done using a Specim IQ portable hyperspectral camera with an internal line-scanning sensor (Specim, Oulu, Finland), which operated in the visible and near-infrared (VNIR) wavelength range 397–1004 nm with 204 spectral bands and 7 nm spectral resolution (full width at half maximum) [40]. The samples were illuminated with 6 quartz halogen lamps in 2 × 3 configuration placed at approximately 20 cm distance from the samples at a 45° angle. The distance and angle of the lamps were selected to maximize signal intensity acquired with the hyperspectral camera. The camera was placed at approximately 23 cm distance from the samples. The distance was measured between the sample surface and the camera lens. The integration time was adjusted to the optimal area suggested by the camera, from which 12 ms was selected to be used for all samples. An externally calibrated 50 % grey diffuse reflectance target (DA75C-1254) was used as the white reference during the experiments, and it was included in the imaging field of view with each sample. The dark reference was supplied by the Specim IQ camera automatically by closing the shutter. The reflectance target and dark current measurements were used to convert the acquired raw signal intensity counts to reflectance values using a linear reflectance transformation [41]. The reflectance values were then -log10 converted into absorbance units [42]. Wavelength variables outside the PAR range (400–700 nm) were removed to eliminate regions that did not have specificity towards photosynthetic pigments, i.e., where the systematic offset in the absorbance signal was generally below pigment absorbance features, and to decrease noise at extreme wavelengths (Fig. S1 in the Supporting information). This reduced the final number of acquired spectral bands to 104 within the PAR range. In this range, the photosynthetic pigments of *Synechocystis* have their in vivo absorbance maxima at ~430–470 and ~675 nm (chlorophyll *a*), ~622 nm (phycocyanin) and ~470–500 nm (carotenoids) [43]. The spatial resolution of the data recorded with the camera was 512 × 512 pixels. From this, the pixels containing the image background, the white reference, and other unwanted regions (i.e., the Petri dish borders and sample edges, where pieces were cut to maintain directionality) were excluded. The omitted pixels were selected by masking the samples with circular areas (~40 cm^2) and subsequently removing the spectra not belonging to the masked area. The sample spectra then consisted of the combined absorbance signal from *Synechocystis* cells within the individual pixel areas of approximately 0.07 mm^2, with the total imaged sample area being ~40 cm^2 and the total number of sample pixels 57,209. Schematic of the hyperspectral imaging setup is shown in Fig. 1.

2.2.3. Determination of chlorophyll a concentration

Chlorophyll *a* (Chl *a*) was spectrophotometrically determined from the reference samples. The results were then used to calibrate the hyperspectral imaging experiments for estimation of Chl *a* from the spectra. Chl *a* was extracted by incubating the 1 cm × 1 cm reference samples in 3 ml of 100 % methanol overnight at 4 °C and in the dark. Afterwards, the samples were centrifuged for 5 min at 4500 *g* and the supernatant was analyzed with Lambda 900 UV/VIS/NIR spectrometer (Perkin Elmer, Waltham, the United States) at 400–1000 nm range. The extracts were handled in dim light to avoid untimely degradation of the light-sensitive pigments. Chl *a* concentration was determined using a specific coefficient (*a*) of 79.24 l g^{-1} cm^{-1} at 665 nm with 100 % methanol as a solvent [30]. Thus, the concentration of Chl *a* was calculated with Eq. (1):

$$C = \frac{(A_{665} - A_{730}) \times V \times 1000}{a \times L} \quad (1)$$

where C is the concentration of Chl *a* in the sample (μg/sample), A_{665} the absorbance of interest at 665 nm, A_{730} the nonspecific absorbance at 730 nm, V the volume of the used solvent (ml), 1000 the required unit conversion factor, *a* the specific coefficient for the used solvent and the wavelength (l g^{-1} cm^{-1}) and L the optical path length (cm). By dividing this result by the area of the hydrogel film sample, Chl *a* concentration per sample area (μg/cm^2) was obtained. Chl *a* concentration was determined according to experimental design from methanol-extracted samples with the number of replicates being 2 for day 1 and 3 for days 10 and 20.

2.3. Data analysis

2.3.1. Factor effects on average object spectra with analysis of variance (ANOVA) simultaneous component analysis (ASCA)

Average spectra were collected from the hyperspectral images of each sample. The average spectra were then decomposed with ANOVA simultaneous component analysis (ASCA) to interpret the effects of the experimental design factors on the sample set [44]. First, we used ASCA to isolate the effects of the controlled factors from the average spectra using the information provided by the experimental design, Eq. (2):

$$\boldsymbol{X_m} = \sum_{i=1}^{p} \boldsymbol{X_i} + \boldsymbol{E} \quad (2)$$

where $\boldsymbol{X_m}$ denoted the mean centered average image spectra, $\boldsymbol{X_i}$ the effect matrices of 4 main and 6 two-factor interaction effects based on the design given in Table S1, and $\boldsymbol{E}$ the model residuals after subtraction of the 10 effects. The sum of squares explained by each factor and their p-values were used to identify significant factor effects and interactions from the spectra. The isolated effects were then decomposed into ASCA scores and loadings according to the general principal components model, Eq. (3):

$$\boldsymbol{X}_i = \sum_{i=1}^{n} \boldsymbol{t_i p_i}^{T} + \boldsymbol{E_n} \quad (3)$$

where $\boldsymbol{X_i}$ denoted an isolated effect matrix from Eq. (2), $\boldsymbol{t_i}$ and $\boldsymbol{p_i}^T$ the orthogonal score and orthonormal loading vectors, respectively, and $\boldsymbol{E}$

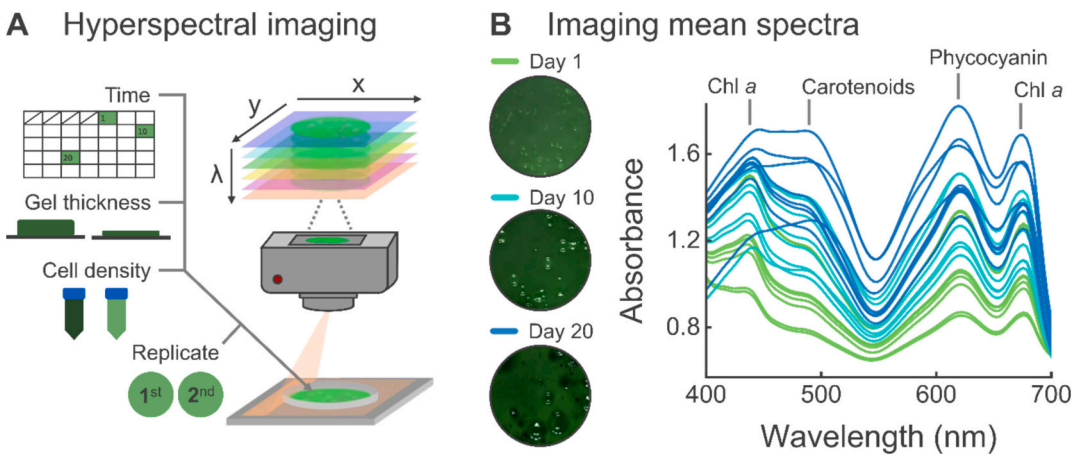

Fig. 1. Schematic of the controlled factors in the experimental design and the hyperspectral imaging setup for monitoring *Synechocystis* immobilized in TCNF hydrogel matrices (A). Average spectra from 57,209 pixels for each of the 24 sample-specific images taken from the immobilized photosynthetic cells (B). The spectra resulting from the samples that were made according to the experimental design are colored by their imaging day. Absorbance maxima of the observed photosynthetic pigments are highlighted in the spectra.

the residuals after n principal components. The residuals $\boldsymbol{E_n}$ from each effect were further projected to the ASCA loadings to describe the natural variation within the factor levels as described previously [45]. The projected scores were then added to the general principal component scores to determine the combined ASCA scores.

2.3.2. Partial least squares (PLS) regression model for quantitative estimation of chlorophyll a from imaging spectra

A partial least squares (PLS) regression model was determined to link the mean centered Chl *a* reference values measured spectrophotometrically from methanol extracts to the mean centered average spectra from the hyperspectral imaging samples. The regression vector $\boldsymbol{b}$ in the general regression equation, Eq. (4):

$$\boldsymbol{y} = \boldsymbol{X}_{\mathrm{m}} \cdot \boldsymbol{b} + \boldsymbol{e} \tag{4}$$

where $\boldsymbol{y}$ denoted a vector consisting of mean centered reference Chl *a* values, $\boldsymbol{X}_{\mathrm{m}}$ the matrix comprised of mean centered sample average spectra, and $\boldsymbol{e}$ the model residuals, was determined using the SIMPLS algorithm [46]. The SIMPLS algorithm determined latent variables iteratively by deflating the covariance of $\boldsymbol{X}_{\mathrm{m}}$ and $\boldsymbol{y}$. The regression vector $\boldsymbol{b}$ (Eq. (4)) was then obtained using the SIMPLS latent variable weights as described by de Jong [46]. Three latent variables were used in the PLS model. The number of latent variables was selected by minimizing the root mean squared error of cross-validation (RMSECV) as shown in Fig. S2 in the Supporting information. The model cross-validation was set up by iteratively dividing the data into random subsets 20 times with 4 splits and 25 % left-out data. The wavelengths important for the model were identified based on the variable importance in the projection (VIP) scores [47], which were determined during the PLS model calculation.

2.3.3. Pixel-specific chlorophyll a analysis with principal component analysis (PCA), clustering and PLS model

The spatial Chl *a* variation was analyzed from the hyperspectral images of the immobilized *Synechocystis* with pixel-specific PCA, clustering and the PLS model calibrated for Chl *a*. The pixel spectra of the second replicates of all samples were first combined into a mosaic, which was then decomposed using PCA. The number of meaningful principal components was chosen by evaluating the differences in the variation explained by each principal component using the scree plot (Fig. S3A in the Supporting information) [48]. The mosaic pixels were then assigned to groups by clustering the score vectors of the selected principal components (Fig. S3B in the Supporting information) using an unsupervised k-means algorithm, where spatial pixels were connected to their corresponding cluster centroids by their squared Euclidean distances in the PCA score space. The number of clusters was selected arbitrarily to show the main differences in the samples. Chl *a* concentrations were then estimated with the PLS model from all pixel spectra that belonged to the same cluster. The average cluster Chl *a* concentrations and their within-cluster standard deviations were calculated from the resulting estimates.

2.3.4. Data analysis software

Image processing and data analyses were performed with in-house MATLAB® (The MathWorks, Inc., Natick, MA, the United States) scripts, which contained functions from PLS toolbox (Eigenvector Research, Inc., Manson, WA, the United States). The VIP scores for the PLS regression model and the ASCA decomposition were determined using PLS toolbox.

3. Results and discussion

3.1. Hyperspectral imaging of Synechocystis immobilized in nanocellulose hydrogel matrices

Images of immobilized *Synechocystis* in TCNF hydrogels were taken with a portable hyperspectral camera according to the experimental design (Fig. 1A). Absorbance spectra were collected from all image pixels, which enabled us to monitor the cells in the whole immobilization matrix area simultaneously. We observed typical features of whole-cell *Synechocystis* absorbance spectra [43] in the acquired images. Specifically, pigments from the phycobilisomes and photosystems produced characteristic wavelength bands corresponding to their in vivo absorbance maxima (Fig. 1B) [43,49]. Chlorophyll *a* (Chl *a*) was observed at ~430–470 and ~675 nm, and carotenoids at ~470–500 nm from the photosystems. From the phycobilisomes, phycocyanin was observed at ~620 nm, whereas allophycocyanin did not have a separate band due to spectral overlap with phycocyanin and Chl *a*.

Light harvesting is the detected pigments' shared biological function, which drives photosynthesis and growth of the cells [49,50]. Cell growth was detected in the hyperspectral imaging experiments as the appearance of visually different areas in the immobilization matrices over time and increasing pigment absorbance (Fig. 1B). The absorbance features may change, however, as the cells react to their environmental conditions. Oxidative stress due to matrix mass transfer limitation has been reported to result in upregulation of hydroxylated carotenoids and Chl *a* degradation in immobilized cultivations [21]. Cells in deeper matrix

layers can also experience self-shading if the cell density is high, which reduces the availability of light for them [23]. This could result in changes in the cells' pigment composition as they adapt to the limited light available for them. Thus, we identified time (the age of cultivation), matrix thickness and immobilized cell density as the key factors potentially causing changes in the immobilized cells during growth and studied their effects with a statistical experimental design. The controlled factors are shown in Fig. 1A, and their levels are given in Table S1 in the Supporting information. By controlling these critical factors, we could non-invasively monitor the cell growth observed in the immobilization matrices with better insight to potential stress.

3.2. Revealing the controlled factors' effects on the immobilized cells absorbance spectra with ASCA

3.2.1. The effect of controlled factors on variation in hyperspectral images

We used a multivariate statistical method, ASCA, to resolve the effects of the controlled factors on the imaging spectra from immobilized *Synechocystis* cells. ASCA first decomposed sample average spectra into factor contributions based on the underlying experimental design and unveiled the percentual effect of each factor and their two-way interactions on the spectral changes with ANOVA. The effects of the factors on the variation in the imaging spectra and their p-values are displayed in Table 1. Factors time, cell density and gel thickness, had statistically significant effects of approximately 58 %, 7 % and 20 %, respectively. This signified that nearly 80 % of the changes in the average imaging spectra from immobilized *Synechocystis* were caused by the age of cultivation and the thickness of the immobilization matrix. The replicate sample for hyperspectral imaging (replicate) and the interaction terms had considerably smaller effects with higher p-values than the first three main factors. Thus, we concentrated on interpreting the effects of time, cell density and gel thickness.

3.2.2. Interpreting the factor effects on the immobilized cells' spectra with ASCA scores and loadings

We interpreted the factor contributions with factor-specific ASCA component scores and loadings. In all ASCA components, positive scores had a positive correlation with positive loadings and vice versa. The resulting factor-specific scores and loadings pointed out areas in the measured spectra that varied between the samples. The scores and loadings for the most influential factors time, cell density and gel thickness are shown in Fig. 2. The scores and loadings for the remaining factors can be found in Fig. S4 in the Supporting information.

Time caused 58 % of the total variation in the absorbance spectra of immobilized *Synechocystis* (Fig. 2A). The scores of this ASCA component separated samples imaged on days 1, 10 and 20 (Fig. 2A, left panel). Furthermore, the samples resembled each other more on day 1 than in 10 or day 20, as indicated by the growing spread of scores with the increasing age of cultivation. These distinctions were interpreted through ASCA component loadings that show the relevance of each wavelength to the scores (Fig. 2A, right panel). The loadings designated that the absorbance of immobilized *Synechocystis* grew over time. Specifically, the wavelengths corresponding to the pigment absorbance maxima highlighted in Fig. 1B were observed to influence the scores the most.

Table 1
The percentual factor effects on the changes observed in the immobilized cells' absorbance spectra as acquired from ASCA. The p-values of the factor effects were obtained using 1000 permutations.

Factor	Effect (%)	p-Value
1 (time)	58	<0.010*
2 (cell density)	7.1	<0.010*
3 (gel thickness)	20	<0.010*
4 (replicate)	1.9	0.081
Interaction of 1 & 2	2.8	0.087
Interaction of 1 & 3	2.4	0.079
Interaction of 1 & 4	1.3	0.30
Interaction of 2 & 3	0.50	0.35
Interaction of 2 & 4	0.47	0.37
Interaction of 3 & 4	0.45	0.34
Residuals	4.3	–

* A statistical significance level of 1 % ($p < 0.010$).

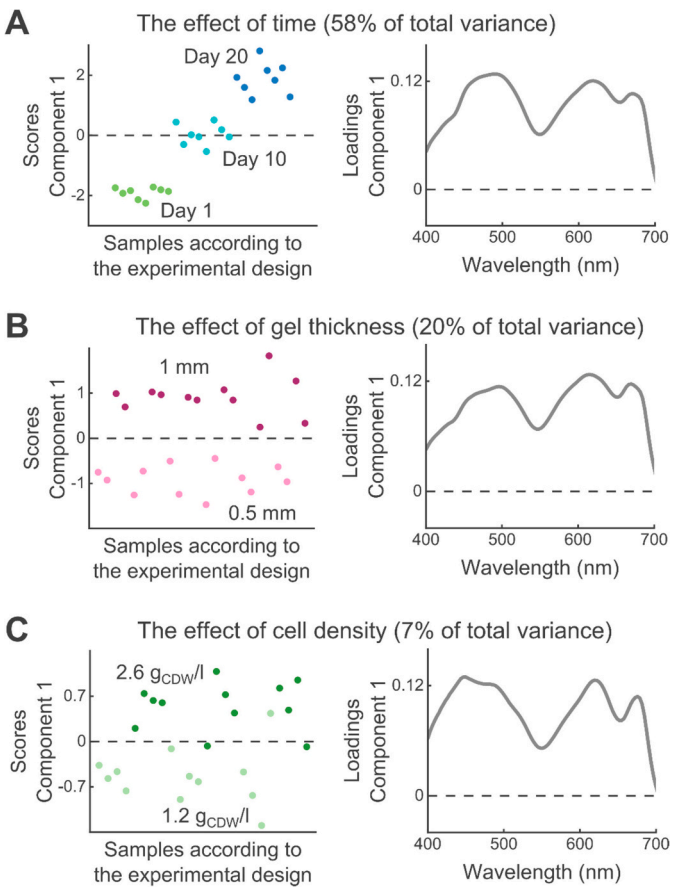

Fig. 2. The first ASCA component scores and loadings for the factors time (A), gel thickness (B), and cell density (C). The panels on the left show the ASCA component score plots, where the 24 samples with immobilized *Synechocystis* are in the order of the experimental design (full design matrix available in Table S1 in the Supporting information). The panels on the right show the corresponding loading plots for interpreting the scores based on the absorbance bands from the imaging spectra obtained from immobilized *Synechocystis*.

ASCA component scores and loadings were also obtained for the other significant factors, gel thickness and cell density that caused 20 % and 7 % of the total variation in the absorbance spectra of immobilized *Synechocystis*, respectively (Fig. 2B and C). The scores for gel thickness (Fig. 2B, left panel) showed that the 1 mm and 0.5 mm immobilization matrices could be distinguished from each other during all imaging days. The loadings indicated that this separation was caused by the thicker matrices having higher pigment absorbance than the thinner matrices (Fig. 2B, right panel). The scores for cell density (Fig. 2C, left panel) also showed that the samples with 1.2 g_{CDW}/l or 2.6 g_{CDW}/l as the initial cell densities could be separated from each other throughout the experiments. This separation was not as clear as for gel thickness, however, which was indicated by higher scatter in the scores and smaller differences between samples. Based on the loadings, the matrices with higher initial cell density had generally higher pigment absorbance than the matrices with lower initial cell density (Fig. 2C, right panel).

The ASCA results showed overall increasing intensity of the pigment absorbance spectra over time, which indicated cell growth in the immobilization matrices. The cell growth was not uniform in the imaged

samples on days 10 and 20, however, as shown by the growing spread of scores (Fig. 2A). We interpreted this to be due to development of spatial differences in the immobilization matrices over time. The second ASCA component of time further explained these differences (Fig. S5 in the Supporting information) by showing that from day 1 to 10 the Chl *a* band at ~430 and phycocyanin band at ~620 nm generally absorbed more than the other pigment absorbance maxima. From day 10 to 20, on the other hand, Chl *a* at ~675 nm and carotenoids at ~500 nm had the highest relative absorbance.

The apparent carotenoid effect at ~500 nm seemed to be emphasized over time in cultivations that had a thick immobilization matrix and a high initial immobilized cell density. This was shown by the ASCA component loadings deviating from the typical wild-type *Synechocystis* absorbance spectrum [43] mostly in the Chl *a*/carotenoid band with spectral overlap at 430–500 nm (Fig. 2, right panels). The interactions of time with cell density (Fig. S4B in the Supporting information) and gel thickness (Fig. S4C in the Supporting information) also described changes in the spectra, although their effects were only 2.8 and 2.4 %, respectively. These interactions showed that the absorbance for Chl *a* at ~430 and ~675 nm and phycocyanin at ~620 nm decreased in relation to other wavelengths over time in samples with a thick matrix or a high cell density, whereas they became more pronounced in samples with a thin matrix or a low cell density.

Elevated absorbance in the carotenoid-associated spectral region can result from stress that could develop over time in the immobilization matrix. Cell growth could cause self-shading that is more severe the deeper the cells are in the immobilization matrix. The cells could then adapt to such light-limitation by producing more accessory pigments, like carotenoids, that assist their light-harvesting [51,52]. In contrast to this hypothesis, the carotenoids were shown earlier to decrease in *Synechocystis* batch suspension cultivations with increasing cell density [53]. However, the movement of immobilized cells is restricted, whereas in suspension cultivations the cells are actively mixed. The restriction of movement could necessitate active production of accessory pigments that enable sufficient light-harvesting in deeper matrix layers, which would explain the differing trend between immobilized and suspension cultivations.

Potential carotenoid upregulation could also stem from mass transfer limitation in the immobilization matrix, which could cause oxidative stress and elevated production of antioxidants, like carotenoids, as a response to such stress [21,22]. This behavior was reported earlier for alginate thin-film cultivations under high light [21]. We also observed earlier that the photosynthetic gas exchange of *Synechocystis* decreased in thick (1 mm) TCNF-based matrices already after five days, which, likewise, could indicate mass transfer limitation [20]. However, we did not use a high light intensity during cultivation here, which should decrease susceptibility of the immobilized cells to oxidative stress due to lower photosynthetic oxygen production in the matrix.

Other reasons for the possible carotenoid effect include contamination of the immobilization matrix with another carotenoid-producing organism that are widely distributed in nature [54,55]. We used axenic cell culture in the experiments and changed fresh sterile media to the matrices during all imaging days to decrease the likelihood of contamination. Furthermore, immobilization protects the cells from environmental conditions [6,9,56], which limits possible contaminations to the surrounding medium rather than to the immobilization matrix itself. Hyperspectral imaging could, however, be readily harnessed for SSPCFs' non-invasive contamination control, which is thus one of the promising future applications for the monitoring method developed here.

We evaluated reliability of the potential carotenoid effect by correlating the carotenoid/Chl *a* ratios from hyperspectral imaging average spectra with the reference ratios that were obtained spectrophotometrically from methanol extracts (Fig. S6 in the Supporting information). The carotenoid/Chl *a* ratios had similar trends overall, which resulted in high positive correlation coefficient between the two methods ($r = 0.81$). However, not all variation in the hyperspectral images' ratios were explained by the reference ratios. This could indicate that the potential carotenoid effect did not develop homogeneously in the immobilization matrices and was not captured by the reference measurements that were conducted for smaller matrix pieces than the imaging. Due to the variation between the two methods, direct quantification of total carotenoids from hyperspectral images was not feasible with the current experimental setup and calculation of total carotenoids from methanol extracts was thus left out. Confirming the carotenoid effect, validating its source and calibrating it for hyperspectral imaging would require further studies with, e.g., chromatographic methods. Although such studies were beyond the scope of this article, they are crucial next steps for developing SSPCFs' stress and contamination monitoring with hyperspectral imaging towards an industrially relevant setting.

More research should also be dedicated to determining how well the current SSPCFs can, in general, scale up to industrial SSPCFs of the future. Here, we systematically extended our knowledge of the effects of time, gel thickness and cell density on immobilized cells' growth at factor levels that result in good SSPCF performance [9,10]. However, we expect that the optimal levels for these factors in future industrial-scale SSPCFs will also depend on the photobioreactor design, scalability of the immobilization matrix, product and producer type, and length of continuous SSPCF operation. Particularly, the length of a production cycle and immobilization matrix dimensions are essential subjects for future optimization. These factors are important because in this study the greater age of cultivation and gel thickness promoted the immobilized cells' growth the most and also contributed to the possible carotenoid effect. The effect of high cell density, too, could be studied further to shed light on light penetration in the immobilization matrices, which is required both for hyperspectral imaging to be applicable and for immobilized cells to thrive in deeper matrix layers. Here, however, we focused next on calibrating hyperspectral imaging for Chl *a* to study the immobilized cells' growth, which was indicated by overall increasing intensity of absorbance spectra over time.

3.3. Non-invasive estimation of chlorophyll a from the immobilized *Synechocystis*

3.3.1. PLS regression model for quantitative chlorophyll a estimation from the hyperspectral images

The average hyperspectral imaging spectra were calibrated against Chl *a* with a PLS regression model so that cell growth could be estimated directly from the spectra (Fig. 3A). The reference Chl *a* concentrations for the calibration of the imaging spectra were obtained spectrophotometrically from methanol extracts, and they are given in Table S2 in the Supporting information. The coefficient of determination (R^2) of the resulting PLS model with three latent variables was 0.90 and the root mean square error of calibration (RMSEC) 0.59 μg/cm^2 (Fig. 3B). Variable importance in the projection (VIP) scores showed that the elevating absorbance of the in vivo pigment absorbance maxima of *Synechocystis* (Fig. 1B) correlated positively with the increasing Chl *a* in the matrices (Fig. 3C).

Pigments other than Chl *a* were also relevant for our PLS model because they are in vivo closely assembled together in phycobilisomes and photosystems [43,49]. The evolution of Chl *a* could be alternatively estimated with spectral indices, where just a few wavelengths sensitive for it would be selected for building a model [13]. Wavelength regions that are not important or have collinearity with the studied variables are typically left out from spectral indices. Disregarding most of the spectra, however, could result in losing information about the potential changes within our immobilized systems. Thus, we decided to keep the full spectra in the PLS model calibrated for Chl *a*.

Changes in the cell immobilization matrices were identified by ASCA to occur over time, and they reduced the fit of our PLS model. The reference measurements had markedly smaller standard deviations and

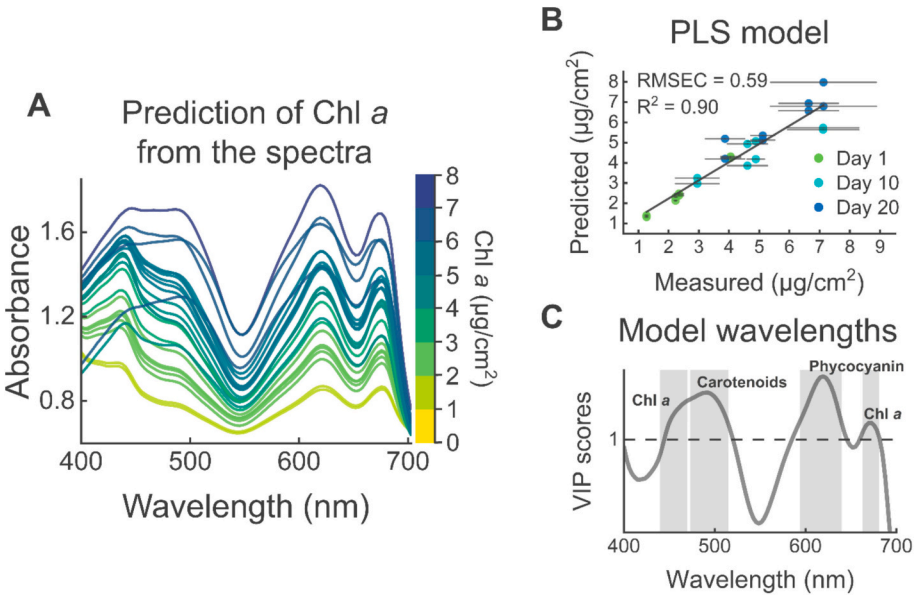

Fig. 3. The imaging average spectra from immobilized *Synechocystis* as colored by the Chl *a* concentrations that were predicted using a PLS regression model (A). A PLS regression model, where the average Chl *a* concentrations from the ex situ reference measurements with methanol extracted pigments (x) were used to predict Chl *a* from each samples' two in situ hyperspectral imaging replicates (y) (B). The variable importance in the projection (VIP) scores showing that the wavelengths corresponding to the in vivo pigment absorbance maxima of *Synechocystis* were influential in the model (VIP scores > 1) (C).

the hyperspectral imaging replicates were more similar to each other on day 1 than in later days (Fig. 3B). As a consequence, the model had increasing prediction errors on days 10 and 20, which indicated that the growth of the immobilized cells was not homogeneous in the matrices. These spatiotemporal differences resulted in the R^2 decreasing from 0.90 to 0.86 and the RMSEC increasing from 0.59 to 0.76 µg/cm^2 after cross-validation. Regardless, our model was almost as accurate as what has been at best reported (R^2 from 0.90 to 0.99) for online monitoring of suspension cultures [29]. Thus, we modeled Chl *a* concentration from the hyperspectral images with a promising correlation and pioneered non-invasive cell growth estimation from the hydrogel immobilization matrices successfully.

3.3.2. *Pixel-specific analysis of chlorophyll a evolution in the immobilization matrices*

Clustering is a useful data analysis method for spatial cyanobacteria population growth monitoring with hyperspectral imaging [15]. Here, we assessed the spatiotemporal changes of the Chl *a* concentration estimated from the immobilized cells at pixel-level using PCA and clustering with the developed PLS model (Fig. 4). First, we decomposed the sample mosaic image with PCA to find the important variations in the pixel dataset. PCA reduced the data dimensions to a single principal component (PC), which explained 97 % of the variation in the data as shown by the scree plot (Fig. S3A in the Supporting information). This let us group the pixels' PC scores (Fig. S3B in the Supporting information) with unsupervised k-means clustering into five clusters that visualized the differences in the immobilization matrices over time (Fig. 4A). The cluster spectra were further analyzed with the developed PLS model, which allowed us to estimate the immobilization matrices' spatial Chl *a* variation over time (Fig. 4B).

On day 1, the thin matrix with low initial cell density comprised its own cluster with estimated average Chl *a* concentration of 1.3 µg/cm^2. Similarly, the thick matrix with high initial cell density was separated to its own cluster with estimated average Chl *a* concentration of 4.5 µg/cm^2. The thin matrix with high cell density and the thick matrix with low cell density had similar immobilized cell densities on day 1, which was shown by the two samples belonging predominantly to the same cluster with estimated average Chl *a* concentration of 2.6 µg/cm^2. On days 10 and 20, all samples showed signs of cell growth with increasing estimated Chl *a* concentrations. The cluster with the highest Chl *a* concentration (9.4 µg/cm^2) was most prominent in the thick matrices on day 20, regardless of the initial cell density, and its formation could

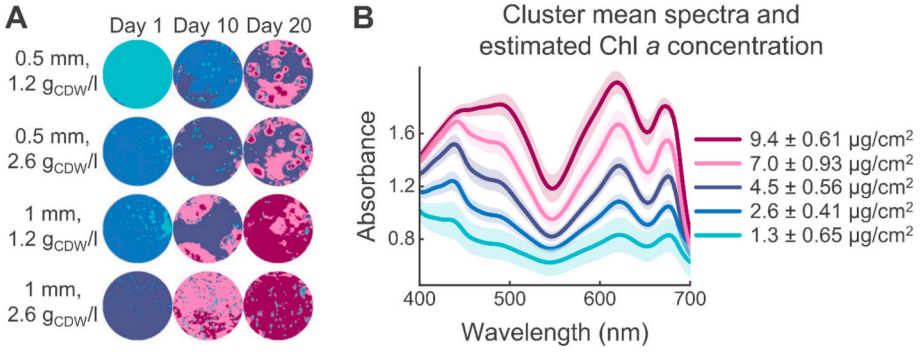

Fig. 4. Pixel-level clustering of the hyperspectral images of immobilized *Synechocystis* taken according to the experimental design (A). Non-invasive estimation of Chl *a* concentration from the cluster spectra using the PLS model calibrated for Chl *a*. Average Chl *a* concentrations and standard deviations were calculated from the clusters' pixel-specific estimates (B).

already be seen regionally during day 10. The thin matrices had small areas belonging to this cluster on day 20 but otherwise had lower Chl *a* concentrations throughout the experiments.

The more time and space the cell had for growing, the higher the estimated Chl *a* concentrations were. The pixel-level transition towards the highest Chl *a* concentrations generally grew outwards from initial points over time. Additionally, small areas with the lowest estimated Chl *a* concentration surrounded the higher Chl *a* areas in the later days. These regions of high reflectance resulted from air bubbles forming in the matrices due to photosynthetic oxygen production, which elevated the matrix surface curvature in the biggest bubbles' boundaries (photograph inset in Fig. 1B). The bubble formation could indicate gas transfer limitation in the mesoporous TCNF hydrogel matrices and result from the heterogeneous pore structure that adapts structurally to cell growth [20]. Specifically, larger pores filled with free water could serve as nuclei for cell growth, which could then slightly expand the visco-elastic TCNF hydrogel network and create more space available for cell growth. This could have led to accumulation of cells and regionally elevated photosynthesis, which resulted in areas with high estimated Chl *a* concentration and bubble formation. The results thus indicate a potential mechanism for cell proliferation over time in TCNF-based immobilization matrices that typically constrain the cell growth [9]. Further studies could target verifying this mechanism and determine if it compromises the mechanical stability of the immobilization matrix during prolonged operation of future larger scale SSPCFs.

4. Conclusions

This study demonstrates a non-invasive approach to follow growth and potential stress of nanocellulose-immobilized *Synechocystis* cells. We monitored spatiotemporal characteristics in the cells' pigment (chlorophyll *a*, phycocyanin and carotenoids) absorbance with controlled hyperspectral imaging. Building on our results, online monitoring of a production task in a continuously operating solid-state photosynthetic cell factory (SSPCF) could be realized in the future. We observed promising correlation (model $R^2 = 0.90$) between hyperspectral imaging and conventional invasive reference method when calibrating a regression model for chlorophyll *a*. However, spatial differences emerged in the matrices via cell growth. These differences mainly resulted from the age of cultivation and the TEMPO-oxidized cellulose nanofiber hydrogel immobilization matrix thickness. Combining the regression model with clustering, we could quantitatively estimate the spatial changes in the immobilized cells' chlorophyll *a* concentrations. In addition to cell growth, we detected possible stress in the immobilization matrices over time via elevated carotenoid absorbance. Validating the carotenoid effect and confirming it as a stress response, however, would require further studies. In the future, hyperspectral imaging will be particularly useful for monitoring product formation, contamination, cell growth or stress of SSPCFs. Quick and non-invasive hyperspectral imaging will also enable the development of SSPCFs towards biointelligent chemical manufacturing, where SSPCFs can be operated with fast feedback control.

CRediT authorship contribution statement

Tuukka Levä: Writing – review & editing, Writing – original draft, Visualization, Validation, Methodology, Investigation, Formal analysis, Data curation. **Ella Mahlamäki:** Writing – review & editing, Visualization, Validation, Software, Methodology, Formal analysis, Data curation. **Sergey Kosourov:** Writing – review & editing, Supervision, Formal analysis. **Yagut Allahverdiyeva:** Writing – review & editing, Supervision, Resources, Project administration, Funding acquisition. **Mikko Mäkelä:** Writing – review & editing, Supervision, Resources, Methodology, Conceptualization. **Tekla Tammelin:** Writing – review & editing, Supervision, Resources, Project administration, Funding acquisition, Conceptualization.

Declaration of competing interest

The authors declare that they have no known competing financial interests or personal relationships that could have appeared to influence the work reported in this paper.

Acknowledgements

This research was financially supported by the Research Council of Finland (AlgaLEAF, project no. 322752/322754); the European Union's Horizon 2020 - Research and Innovation Framework Programme (FuturoLEAF, grant agreement 899576); and the Research Council of Finland's Flagship Programme (Competence Center for Materials Bioeconomy, FinnCERES, funding decision no. 345556). We thank Tuomas Sormunen (VTT Technical Research Centre of Finland) for the access to Specim IQ hyperspectral camera and Tuuli Virkkala (VTT Technical Research Centre of Finland) for help with hydrogel sample preparation.

Appendix A. Supplementary data

Table S1: summary of the experimental design; Fig. S1: average VNIR absorbance spectra from hyperspectral imaging and the PAR region included in further analysis; Fig. S2: graph of RMSEC and RMSECV for selecting the number of latent variables in the PLS model; Fig. S3: the scree plot and the first principal component for pixel-level clustering; Fig. S4: the first ASCA components of the main factor replicate and the interaction terms; Fig. S5: the second ASCA component of the main factor time; Fig. S6: comparison of the carotenoid/Chl *a* ratios of average imaging spectra and reference spectra from methanol extracts; Table S2: spectrophotometrically measured reference Chl *a* concentrations. Supplementary data to this article can be found online at https://doi.org/10.1016/j.algal.2025.104090.

Data availability

Data will be made available on request.

References

[1] A. Hitchcock, C.N. Hunter, D.P. Canniffe, Progress and challenges in engineering cyanobacteria as chassis for light-driven biotechnology, Microb. Biotechnol. 13 (2020) 363–367, https://doi.org/10.1111/1751-7915.13526.
[2] R. Miao, H. Xie, X. Liu, P. Lindberg, P. Lindblad, Current processes and future challenges of photoautotrophic production of acetyl-CoA-derived solar fuels and chemicals in cyanobacteria, Curr. Opin. Chem. Biol. 59 (2020) 69–76, https://doi.org/10.1016/j.cbpa.2020.04.013.
[3] V. Siitonen, A. Probst, G. Tóth, R. Kourist, M. Schroda, S. Kosourov, Y. Allahverdiyeva, Engineered green alga Chlamydomonas reinhardtii as a whole-cell photosynthetic biocatalyst for stepwise photoproduction of H2 and ϵ-caprolactone, Green Chem. 25 (2023) 5945–5955, https://doi.org/10.1039/d3gc01400b.
[4] E. Erdem, L. Malihan-Yap, L. Assil-Companioni, H. Grimm, G.D. Barone, C. Serveau-Avesque, A. Amouric, K. Duquesne, V. De Berardinis, Y. Allahverdiyeva, V. Alphand, R. Kourist, Photobiocatalytic oxyfunctionalization with high reaction rate using a Baeyer-Villiger monooxygenase from Burkholderia xenovorans in metabolically engineered cyanobacteria, ACS Catal. 12 (2022) 66–72, https://doi.org/10.1021/acscatal.1c04555.
[5] S.N. Kosourov, M. Seibert, Hydrogen photoproduction by nutrient-deprived Chlamydomonas reinhardtii cells immobilized within thin alginate films under aerobic and anaerobic conditions, Biotechnol. Bioeng. 102 (2009) 50–58, https://doi.org/10.1002/bit.22050.
[6] M. Jämsä, S. Kosourov, V. Rissanen, M. Hakalahti, J. Pere, J.A. Ketoja, T. Tammelin, Y. Allahverdiyeva, Versatile templates from cellulose nanofibrils for photosynthetic microbial biofuel production, J. Mater. Chem. A 6 (2018) 5825–5835, https://doi.org/10.1039/c7ta11164a.
[7] S. Vajravel, S. Sirin, S. Kosourov, Y. Allahverdiyeva, Towards sustainable ethylene production with cyanobacterial artificial biofilms, Green Chem. 22 (2020) 6404–6414, https://doi.org/10.1039/d0gc01830a.
[8] C. Bailliez, C. Largeau, C. Berkaloff, E. Casadevall, Immobilization of Botryococcus braunii in alginate: influence on chlorophyll content, photosynthetic activity and degeneration during batch cultures, Appl. Microbiol. Biotechnol. 23 (1986) 361–366, https://doi.org/10.1007/BF00257033.
[9] V. Rissanen, S. Vajravel, S. Kosourov, S. Arola, E. Kontturi, Y. Allahverdiyeva, T. Tammelin, Nanocellulose-based mechanically stable immobilization matrix for

enhanced ethylene production: a framework for photosynthetic solid-state cell factories, Green Chem. 23 (2021) 3715–3724, https://doi.org/10.1039/D1GC00502B.
[10] T. Virkkala, S. Kosourov, V. Rissanen, V. Siitonen, S. Arola, Y. Allahverdiyeva, T. Tammelin, Bioinspired mechanically stable all-polysaccharide based scaffold for photosynthetic production, J. Mater. Chem. B (2023) 8788–8803, https://doi.org/10.1039/d3tb00919j.
[11] S. Kosourov, T. Tammelin, Y. Allahverdiyeva, Engineered biocatalytic architecture for enhanced light utilisation in algal H2 production, Energy Environ. Sci. 18 (2025) 937–947, https://doi.org/10.1039/D4EE03075C.
[12] R. Miehe, T. Bauernhansl, O. Schwarz, A. Traube, A. Lorenzoni, L. Waltersmann, J. Full, J. Horbelt, A. Sauer, The biological transformation of the manufacturing industry - envisioning biointelligent value adding, Procedia CIRP 72 (2018) 739–743, https://doi.org/10.1016/j.procir.2018.04.085.
[13] P. Salmi, M.A. Eskelinen, M.T. Leppänen, I. Pölönen, Rapid quantification of microalgae growth with hyperspectral camera and vegetation indices, Plants 10 (2021) 1–12, https://doi.org/10.3390/plants10020341.
[14] P. Salmi, M. Calderini, S. Pääkkönen, S. Taipale, I. Pölönen, Assessment of microalgae species, biomass, and distribution from spectral images using a convolution neural network, J. Appl. Phycol. 34 (2022) 1565–1575, https://doi.org/10.1007/s10811-022-02735-w.
[15] F. Rodríguez Lorenzo, M. Placer Lorenzo, L. Herrero Castilla, J.A. Álvarez Rodríguez, S. Iglesias, S. Gómez, J.M. Fernández Montenegro, E. Rueda, R. Diez-Montero, J. Garcia, E. Gonzalez-Flo, Monitoring PHB production in Synechocystis sp. with hyperspectral images, Water Sci. Technol. 86 (2022) 211–226, https://doi.org/10.2166/wst.2022.194.
[16] N.R. Moheimani, M.A. Borowitzka, A. Isdepsky, S.F. Sing, Standard methods for measuring growth of algae and their composition, in: M.A. Borowitzka, N. R. Moheimani (Eds.), Algae for Biofuels and Energy, Springer Netherlands, Dordrecht, 2013, pp. 265–284, https://doi.org/10.1007/978-94-007-5479-9_16.
[17] M.C. Flickinger, J.L. Schottel, D.R. Bond, A. Aksan, L.E. Scriven, Painting and printing living bacteria: engineering nanoporous biocatalytic coatings to preserve microbial viability and intensify reactivity, Biotechnol. Prog. 23 (2007) 2–17, https://doi.org/10.1021/bp060347r.
[18] J. Lee, M.J. Cuddihy, N.A. Kotov, Three-dimensional cell culture matrices: state of the art, Tissue Eng. - Part B Rev. 14 (2008) 61–86, https://doi.org/10.1089/teb.2007.0150.
[19] E. Eroglu, S.M. Smith, C.L. Raston, Application of various immobilization techniques for algal bioprocesses, in: N.R. Moheimani, M.P. McHenry, K. de Boer, P.A. Bahri (Eds.), Biomass Biofuels From Microalgae, Springer, Cham, 2015, pp. 19–44, https://doi.org/10.1007/978-3-319-16640-7_2.
[20] T. Levä, V. Rissanen, L. Nikkanen, V. Siitonen, M. Heilala, J. Phiri, T.C. Maloney, S. Kosourov, Y. Allahverdiyeva, M. Mäkelä, T. Tammelin, Mapping nanocellulose- and alginate-based photosynthetic cell factory scaffolds: interlinking porosity, wet strength, and gas exchange, Biomacromolecules 24 (2023) 3484–3497, https://doi.org/10.1021/acs.biomac.3c00261.
[21] S. Kosourov, G. Murukesan, M. Seibert, Y. Allahverdiyeva, Evaluation of light energy to H2 energy conversion efficiency in thin films of cyanobacteria and green alga under photoautotrophic conditions, Algal Res. 28 (2017) 253–263, https://doi.org/10.1016/j.algal.2017.09.027.
[22] A. Latifi, M. Ruiz, C.C. Zhang, Oxidative stress in cyanobacteria, FEMS Microbiol. Rev. 33 (2009) 258–278, https://doi.org/10.1111/j.1574-6976.2008.00134.x.
[23] L. Assil-Companioni, H.C. Büchsenschütz, D. Solymosi, N.G. Dyczmons-Nowaczyk, K.K.F. Bauer, S. Wallner, P. MacHeroux, Y. Allahverdiyeva, M.M. Nowaczyk, R. Kourist, Engineering of NADPH supply boosts photosynthesis-driven biotransformations, ACS Catal. 10 (2020) 11864–11877, https://doi.org/10.1021/acscatal.0c02601.
[24] H.K. Lichtenthaler, J.A. Miehé, Fluorescence imaging as a diagnostic tool for plant stress, Trends Plant Sci. 2 (1997) 316–320, https://doi.org/10.1016/S1360-1385(97)89954-2.
[25] W.F.J. Vermaas, J.A. Timlin, H.D.T. Jones, M.B. Sinclair, L.T. Nieman, S. W. Hamad, D.K. Melgaard, D.M. Haaland, In vivo hyperspectral confocal fluorescence imaging to determine pigment localization and distribution in cyanobacterial cells, Proc. Natl. Acad. Sci. USA 105 (2008) 4050–4055, https://doi.org/10.1073/pnas.0708090105.
[26] K. Schulze, D.A. López, U.M. Tillich, M. Frohme, A simple viability analysis for unicellular cyanobacteria using a new autofluorescence assay, automated microscopy, and ImageJ, BMC Biotechnol. 11 (2011), https://doi.org/10.1186/1472-6750-11-118.
[27] K. Schulze, I. Lang, H. Enke, D. Grohme, M. Frohme, The use of fluorescence microscopy and image analysis for rapid detection of non-producing revertant cells of *Synechocystis* sp. PCC6803 and *Synechococcus* sp. PCC7002, BMC Res. Notes 8 (2015) 1–11, https://doi.org/10.1186/s13104-015-1112-1.
[28] B. Fernández-Marín, J.I. García-Plazaola, A. Hernández, R. Esteban, Plant photosynthetic pigments: methods and tricks for correct quantification and identification, in: A.M. Sánchez-Moreiras, M.J. Reigosa (Eds.), Adv. Plant Ecophysiol. Tech, Springer International Publishing, Cham, 2018, pp. 29–50, https://doi.org/10.1007/978-3-319-93233-0_3.
[29] I. Havlik, S. Beutel, T. Scheper, K.F. Reardon, On-line monitoring of biological parameters in microalgal bioprocesses using optical methods, Energies 15 (2022) 1–27, https://doi.org/10.3390/en15030875.
[30] H.K. Lichtenthaler, Chlorophylls and carotenoids: pigments of photosynthetic biomembranes, Methods Enzymol. 148 (1987) 350–382, https://doi.org/10.1016/0076-6879(87)48036-1.
[31] K. Maxwell, G.N. Johnson, Chlorophyll fluorescence—a practical guide, J. Exp. Bot. 51 (2000) 659–668, https://doi.org/10.1093/jexbot/51.345.659.
[32] J. Peñuelas, L. Filella, Visible and near-infrared reflectance techniques for diagnosing plant physiological status, Trends Plant Sci. 3 (1998) 151–156, https://doi.org/10.1016/S1360-1385(98)01213-8.
[33] G.A. Blackburn, Hyperspectral remote sensing of plant pigments, J. Exp. Bot. 58 (2007) 855–867, https://doi.org/10.1093/jxb/erl123.
[34] Z. Yang, M. Reiter, N. Munyei, Estimation of chlorophyll-a concentrations in diverse water bodies using ratio-based NIR/Red indices, Remote Sens. Appl. Soc. Environ. 6 (2017) 52–58, https://doi.org/10.1016/j.rsase.2017.04.004.
[35] R.E. O'Shea, N. Pahlevan, B. Smith, M. Bresciani, T. Egerton, C. Giardino, L. Li, T. Moore, A. Ruiz-Verdu, S. Ruberg, S.G.H. Simis, R. Stumpf, D. Vaičiūtė, Advancing cyanobacteria biomass estimation from hyperspectral observations: demonstrations with HICO and PRISMA imagery, Remote Sens. Environ. 266 (2021), https://doi.org/10.1016/j.rse.2021.112693.
[36] M. Manley, Near-infrared spectroscopy and hyperspectral imaging: non-destructive analysis of biological materials, Chem. Soc. Rev. 43 (2014) 8200–8214, https://doi.org/10.1039/c4cs00062e.
[37] R. Rippka, J. Deruelles, J.B. Waterbury, Generic assignments, strain histories and properties of pure cultures of cyanobacteria, J. Gen. Microbiol. 111 (1979) 1–61, https://doi.org/10.1099/00221287-111-1-1.
[38] T. Saito, Y. Nishiyama, J.L. Putaux, M. Vignon, A. Isogai, Homogeneous suspensions of individualized microfibrils from TEMPO-catalyzed oxidation of native cellulose, Biomacromolecules 7 (2006) 1687–1691, https://doi.org/10.1021/bm060154s.
[39] SCAN-CM 65:02, Pulp – Total Acidic Group Content: Conductometric Titration Method, Scand. Pulp, Pap. Board Test. Comm, 2002, pp. 1–4.
[40] J. Behmann, K. Acebron, D. Emin, S. Bennertz, S. Matsubara, S. Thomas, D. Bohnenkamp, M.T. Kuska, J. Jussila, H. Salo, A.K. Mahlein, U. Rascher, Specim IQ: Evaluation of a new, miniaturized handheld hyperspectral camera and its application for plant phenotyping and disease detection, Sensors 18 (2) (2018) 441, https://doi.org/10.3390/s18020441.
[41] J. Burger, P. Geladi, Hyperspectral NIR image regression part I: calibration and correction, J. Chemom. 19 (2005) 355–363, https://doi.org/10.1002/cem.938.
[42] B. Boldrini, W. Kessler, K. Rebner, R.W. Kessler, Hyperspectral imaging: a review of best practice, performance and pitfalls for in-line and on-line applications, J. Near Infrared Spectrosc. 20 (2012) 483–508. https://opg.optica.org/jnirs/abstract.cfm?URI=jnirs-20-5-483.
[43] D. Fuente, D. Lazar, J.V. Oliver-Villanueva, J.F. Urchueguía, Reconstruction of the absorption spectrum of Synechocystis sp. PCC 6803 optical mutants from the in vivo signature of individual pigments, Photosynth. Res. 147 (2021) 75–90, https://doi.org/10.1007/s11120-020-00799-8.
[44] C. Bertinetto, J. Engel, J. Jansen, ANOVA simultaneous component analysis: a tutorial review, Anal. Chim. Acta X 6 (2020), https://doi.org/10.1016/j.acax.2020.100061.
[45] G. Zwanenburg, H.C.J. Hoefsloot, J.A. Westerhuis, J.J. Jansen, A.K. Smilde, ANOVA–principal component analysis and ANOVA–simultaneous component analysis: a comparison, J. Chemom. 25 (2011) 561–567, https://doi.org/10.1002/cem.1400.
[46] S. de Jong, SIMPLS: an alternative approach to partial least squares regression, Chemom. Intell. Lab. Syst. 18 (1993) 251–263, https://doi.org/10.1016/0169-7439(93)85002-X.
[47] I.G. Chong, C.H. Jun, Performance of some variable selection methods when multicollinearity is present, Chemom. Intell. Lab. Syst. 78 (2005) 103–112, https://doi.org/10.1016/j.chemolab.2004.12.011.
[48] P. Geladi, Chemometrics in spectroscopy. Part 1. Classical chemometrics, Spectrochim. Acta B At. Spectrosc. 58 (2003) 767–782, https://doi.org/10.1016/S0584-8547(03)00037-5.
[49] C. Deepika, J. Wolf, J. Roles, I. Ross, B. Hankamer, Sustainable production of pigments from cyanobacteria, Adv. Biochem. Eng. Biotechnol. 183 (2023) 171–251, https://doi.org/10.1007/10_2022_211.
[50] D.K. Saini, S. Pabbi, P. Shukla, Cyanobacterial pigments: perspectives and biotechnological approaches, Food Chem. Toxicol. 120 (2018) 616–624, https://doi.org/10.1016/j.fct.2018.08.002.
[51] H.A. Frank, R.J. Cogdell, Carotenoids in photosynthesis, Photochem. Photobiol. 63 (1996) 257–264.
[52] G. Britton, Functions of intact carotenoids, in: G. Britton, S. Liaaen-Jensen, H. Pfander (Eds.), Carotenoids, Vol. 4 Nat. Funct, 1st ed., Birkhäuser Basel, Basel, 2008, pp. 189–212, https://doi.org/10.1007/978-3-7643-7499-0.
[53] T. Zavřel, H. Schoffman, M. Lukeš, J. Fedorko, N. Keren, J. Červený, Monitoring fitness and productivity in cyanobacteria batch cultures, Algal Res. 56 (2021), https://doi.org/10.1016/j.algal.2021.102328.
[54] H. Du, N. Jiao, Y. Hu, Y. Zeng, Diversity and distribution of pigmented heterotrophic bacteria in marine environments, FEMS Microbiol. Ecol. 57 (2006) 92–105, https://doi.org/10.1111/j.1574-6941.2006.00090.x.
[55] J. Alcaíno, M. Baeza, V. Cifuentes, Carotenoid distribution in nature, in: C. Stange (Ed.), Carotenoids: Natural Biosynthesis, Regulation, and Function, Springer International Publishing, Cham, 2016, pp. 3–33, https://doi.org/10.1007/978-3-319-39126-7_1.
[56] D.J. Dickson, C.J. Page, R.L. Ely, Photobiological hydrogen production from Synechocystis sp. PCC 6803 encapsulated in silica sol-gel, Int. J. Hydrog. Energy 34 (2009) 204–215, https://doi.org/10.1016/j.ijhydene.2008.10.021.